

RESEARCH ARTICLE | JULY 11 2023

Flow-field reconstruction in rotating detonation combustor based on physics-informed neural network

Wang Xutun (王绪墩)  ; Wen Haocheng (闻浩诚)   ; Hu Tong (胡桐); Wang Bing (王兵)  



Physics of Fluids 35, 076109 (2023)
<https://doi.org/10.1063/5.0154979>



Articles You May Be Interested In

Combustion mode time-series prediction in rotating detonation combustor based on predictor of encoder transformer

Physics of Fluids (September 2025)

Observation-guided generative flow field reconstruction of rotating detonation combustor

Physics of Fluids (November 2025)

Propagation and heat release characteristics of rotating detonation in a ramjet engine with a divergent combustor

Physics of Fluids (February 2025)



Physics of Fluids
Special Topics
Open for Submissions

[Learn More](#)

AIP Publishing

Flow-field reconstruction in rotating detonation combustor based on physics-informed neural network

Cite as: Phys. Fluids **35**, 076109 (2023); doi: 10.1063/5.0154979

Submitted: 17 April 2023 · Accepted: 21 June 2023 ·

Published Online: 11 July 2023



View Online



Export Citation



CrossMark

Xutun Wang (王绪墩),¹ Haocheng Wen (闻浩诚),^{1,a} Tong Hu (胡桐),² and Bing Wang (王兵)^{1,a}

AFFILIATIONS

¹School of Aerospace Engineering, Tsinghua University, Beijing 100084, China

²Shanghai Jiao Tong University Sichuan Research Institute, Chengdu, Sichuan 610042, China

^aAuthors to whom correspondence should be addressed: haochengwenson@126.com and wbing@tsinghua.edu.cn

ABSTRACT

The flow-field reconstruction of a rotating detonation combustor (RDC) is essential to understand the stability mechanism and performance of rotating detonation engines. This study embeds a reduced-order model of an RDC into a neural network (NN) to construct a physics-informed neural network (PINN) to achieve the full-dimensional high-resolution reconstruction of the combustor flow field based on partially observed data. Additionally, the unobserved physical fields are extrapolated through the NN-embedded physical model. The influence of the residual point sampling strategy and observation point spatial-temporal sampling resolution on the reconstruction results are studied. As a surrogate model of the RDC, the PINN fills the gap that traditional computational fluid dynamics methods have difficulty solving, such as inverse problems, and has engineering value for the flow-field reconstruction of RDCs.

Published under an exclusive license by AIP Publishing. <https://doi.org/10.1063/5.0154979>

I. INTRODUCTION

Rotating detonation engines (RDEs) have attracted significant attention in recent years as promising propulsion systems due to their potential for high efficiency. Unlike conventional engines based on deflagration combustion, detonative propulsion achieves greater thermodynamic efficiency^{1,2} and inherent pressure-gain properties.³ Over the past decade, various attempts have been made to design new propulsion systems based on detonation, such as pulsed detonation engines (PDEs),⁴ oblique detonation engines (ODEs),⁵ and RDEs.^{6,7} Among these systems, RDEs show promising results for future aerospace propulsion systems due to their suitability over a wide speed range compared to ODEs and their ability to provide stable thrust compared to PDEs.⁸

However, there are still some crucial problems to solve before the engineering application of RDEs, including the complex combustion modes and instabilities.^{9–12} Obtaining high-resolution flow fields inside the combustor helps solve these problems. However, it is challenging to obtain full-dimensional high-resolution physical fields based on existing measurements adopted for rotating detonation combustors (RDCs). First, the spatiotemporal resolution is limited due to the number of installed sensors and their sampling frequency.¹³

Moreover, only some physical variables, such as pressure or temperature, can be measured directly inside the combustor. At the same time, it is difficult to quantitatively measure the physical variables associated with chemical reactions. Thus, only partial dimensional low-resolution physical fields can be obtained, but full-dimensional high-resolution physical fields are needed. Filling in missing values and dimensions while maintaining physical consistency remains a typical inverse problem, which is difficult to solve using traditional computational fluid dynamics (CFD) methods.^{14–16}

Inspired by the success of machine learning in fluid mechanics,^{17,18} this paper builds neural network (NN)-embed physical knowledge, namely a physics-informed neural network (PINN), to estimate the continuous physical fields from discrete sensor data and extrapolate unmeasured physical quantities. With recent advances in machine learning^{19–21} and their great success in assisting scientific discovery,^{22–28} physics-informed machine learning²⁹ has highlighted the importance of integrating physical knowledge into machine learning methods when applied to handle scientific or engineering problems. There are three perspectives to integrating physical knowledge into machine learning: observational bias, inductive bias, and learning bias.²⁹ This paper focuses on learning bias. Since Raissi³⁰ first proposed PINN in 2019, it has been widely applied in various fields, such

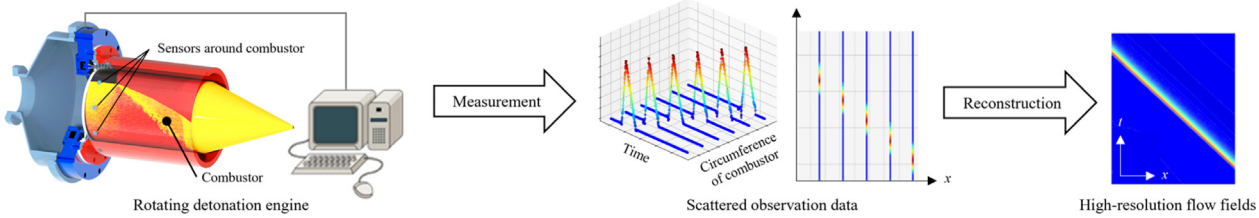


FIG. 1. Flow-field reconstruction problem for a rotating detonation combustor (RDC). The scattered data as obtained from the circumferentially placed sensors are used to reconstruct the high-resolution physical fields inside the RDC.

as physics, chemistry, medicine, and engineering. Fluid mechanics has been a key application domain for PINN. Numerous studies^{16,31–36} have considered solving flow problems by introducing physical models into NNs and incorporating governing equations into the loss functions.

This study focuses on the flow-field reconstruction of an RDC, as illustrated in Fig. 1. The time sequence of discrete data for the pressure, temperature, and velocity fields are obtained from the RDC based on fixed sensors placed circumferentially. With scattered observed data, we propose a PINN method incorporating deep learning with physical knowledge to reconstruct high-resolution physical fields and extrapolate unobserved physical fields inside the RDC. The method is based on a simplified model of the RDC,³⁷ which provides consistent physics in the reconstruction results.

This paper is arranged as follows: Section II provides a detailed description of the PINN method used in the study, including the data acquisition and training parameters. Section III presents the reconstruction results and discussion. Finally, Sec. IV presents the conclusions.

II. METHODOLOGY

A. PINN

The PINN is a deep network that combines a NN with the governing equations of a physical system. The PINN incorporates prior knowledge of the system physics by integrating the nonlinear partial differential equation into the NN loss function.³⁰ The central concept of the PINN is to approximate the spatiotemporal solution of differential equations using a fully connected neural network (FNN). The FNN is composed of one input layer, one output layer, and several hidden layers.³⁸ The external signals are received by the input layer, processed by the hidden layers, and output by the output layer. It is assumed that there are $k-1$ hidden layers in the middle with N_L neural nodes in the L th hidden layer. The input of L th hidden layer is represented by $\mathbf{x}^{L-1} \in R^{N_{L-1}}$, and its output is represented by $\mathbf{x}^L \in R^{N_L}$. These satisfy the following relation:

$$\mathbf{x}^L = \sigma(\mathbf{W}^L \mathbf{x}^{L-1} + \mathbf{b}^L), \quad (1)$$

where $\sigma(\cdot)$ is the activation function, $\mathbf{W}^L \in R^{N_L \times N_{L-1}}$ is the weight term, and $\mathbf{b}^L \in R^{N_L}$ is the bias term. The linear transformation $\varphi_L(\cdot)$ in the L th layer is defined as

$$\mathbf{W}^L \mathbf{x}^{L-1} + \mathbf{b}^L = \varphi_L(\mathbf{x}^{L-1}). \quad (2)$$

If the initial input is \mathbf{x}^0 and the final output is \mathbf{x}^L , then,

$$\mathbf{x}^L = F_{NN}(\mathbf{x}^0) = (\varphi_L \circ \sigma \circ \varphi_{L-1} \circ \dots \circ \sigma \circ \varphi_1)(\mathbf{x}^0), \quad (3)$$

where the transform F_{NN} is determined by $\mathbf{W}^L, \mathbf{W}^{L-1} \dots \mathbf{W}^1$ and $\mathbf{b}^L, \mathbf{b}^{L-1} \dots \mathbf{b}^1$, as shown in Fig. 2. Generally, a partial differential equation and its boundary condition take the form

$$\begin{aligned} L(\mathbf{u}) &= a, \mathbf{x} \in \Omega \\ B(\mathbf{u}) &= 0, \mathbf{x} \in \partial\Omega, \end{aligned} \quad (4)$$

where $L(\cdot)$ is a nonlinear differential operator, $B(\cdot)$ is a boundary operator, and $\mathbf{u}(\mathbf{x})$ describes the latent solution governed by the partial differential equation system.

According to the universal approximation theorem,³⁹ an FNN can approximate the solution of partial differential equations. The unknown solution can be represented as

$$\mathbf{u} = F_{NN}(\mathbf{x}, \theta), \quad (5)$$

where \mathbf{x} and \mathbf{u} , respectively, denote the inputs and outputs of the NN, and θ denotes the trainable parameters. For the fully connected network, θ includes the weights and biases of multiple hidden layers. The automatic differentiation characteristics of the NN⁴⁰ indicate that the error terms can be integrated into the loss function. Thus, the PINN can be trained by minimizing the loss function,

$$L(\theta) = w_r L_r(\theta) + w_{bc} L_{bc}(\theta), \quad (6)$$

$$L_r(\theta) = \frac{1}{N_r} \sum_{i=1}^{N_r} \|L(F_{NN}(\mathbf{x}_r^i, \theta)) - a\|_2^2, \quad (7)$$

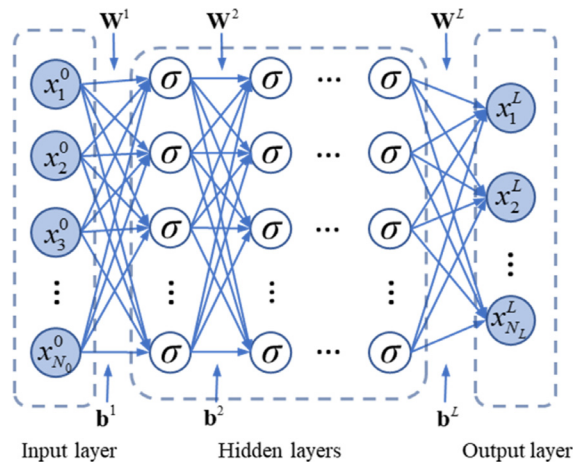


FIG. 2. Structure of an FNN composed of one input layer, one output layer, and several hidden layers.

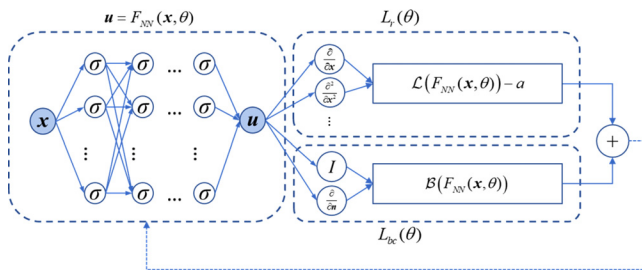


FIG. 3. Structure of a typical PINN composed of an FNN part (left) and a physics-informed part (right). The physics-informed part enforces the FNN outputs as partial differential equation constraints.

$$L_{bc}(\theta) = \frac{1}{N_{bc}} \sum_{i=1}^{N_{bc}} \|B(F_{NN}(\mathbf{x}_{bc}^i, \theta))\|_2^2, \quad (8)$$

where $L_r(\theta)$ describes the unsupervised loss of residuals from the differential equation, and $L_{bc}(\theta)$ describes the supervised loss of the partial differential equation's boundary condition. The hyper-parameters $\{w_r, w_{bc}\}$ are used to balance the learning rate during training. The $\{\mathbf{x}_r^i\}_{i=1}^{N_r}$ and $\{\mathbf{x}_{bc}^i\}_{i=1}^{N_{bc}}$ are the calculation points sampled from the computational domain.

Figure 3 illustrates the general structure of the PINN, consisting of two main components: a standard FNN and a physics-informed part. The standard FNN predicts the outputs of the physics system as governed by the partial differential equation. The physics-informed part of the network enforces the partial differential equation constraints using automatic differentiation to compute the network gradients with respect to the inputs. Minimizing the loss function through gradient-based optimizers until the loss is smaller than a threshold ε allows approximating the solution of the partial differential equation.

B. PINN for rotating detonation combustor

In a typical annular RDC, the system reaches a quasi-steady state when the highly nonlinear combustion instability associated with the

periodic geometry becomes saturated.⁴¹ However, as both the fastest and slowest physics need to be considered simultaneously,⁴² direct simulations are usually computationally expensive. Consequentially, several existing reduced-order modeling approaches reduce computational costs. This study uses the lumped-volume combustor model developed by Koch and Kutz.³⁷

The model based on a generic RDE annular combustor is shown in Fig. 4(a). The model combines the aspects of the rotating detonation analog with the one-dimensional (1D) Euler equations for the inviscid compressible flow. A lumped-volume combustor model is used for the spatially extended model formulation in Fig. 4(b) to model flow from the injector to the combustor exit at each spatial point along the 1D computational domain. The Euler equations model the fluid flow along the circumference of the annulus inside the combustor. The two models are coupled via source terms for the 1D Euler equations, and the nondimensional 1D governing equation is Eq. (9). We solve the model to attain the detailed spatiotemporal propagation of the detonation wave as Fig. 4(c),

$$\frac{\partial}{\partial t} \begin{bmatrix} \rho \\ \rho u \\ E \\ \rho \lambda \end{bmatrix} + \frac{\partial}{\partial x} \begin{bmatrix} \rho u \\ \rho u^2 + p \\ u(E+p) \\ \rho u \lambda \end{bmatrix} = \begin{bmatrix} \alpha(A^+H - A^- \sqrt{p\rho}) \\ 0 \\ \frac{\alpha}{\gamma-1}(A^+H - TA^- \sqrt{p\rho}) + \dot{\omega}q \\ \dot{\omega} - \rho\beta H + \alpha\lambda(A^+H - A^- \sqrt{p\rho}) \end{bmatrix}. \quad (9)$$

In Eq. (9), A^+ and A^- are the non-dimensional injection area and notional geometric throat area, and H is the injection sub-model, which provides the relationship between the mass flow rate and combustor pressure as

$$H(p) = \mathbf{H}(1-p) \left(1 - \mathbf{H}(p-X) \frac{p-X}{1-X} \right), \quad (10)$$

$$X = \left(1 + \left(\frac{\gamma-1}{2} \right)^{-\frac{\gamma}{\gamma-1}} \right),$$

where \mathbf{H} is the Heaviside step function. In Eq. (9), E is the total energy, including the internal and kinetic energy components,

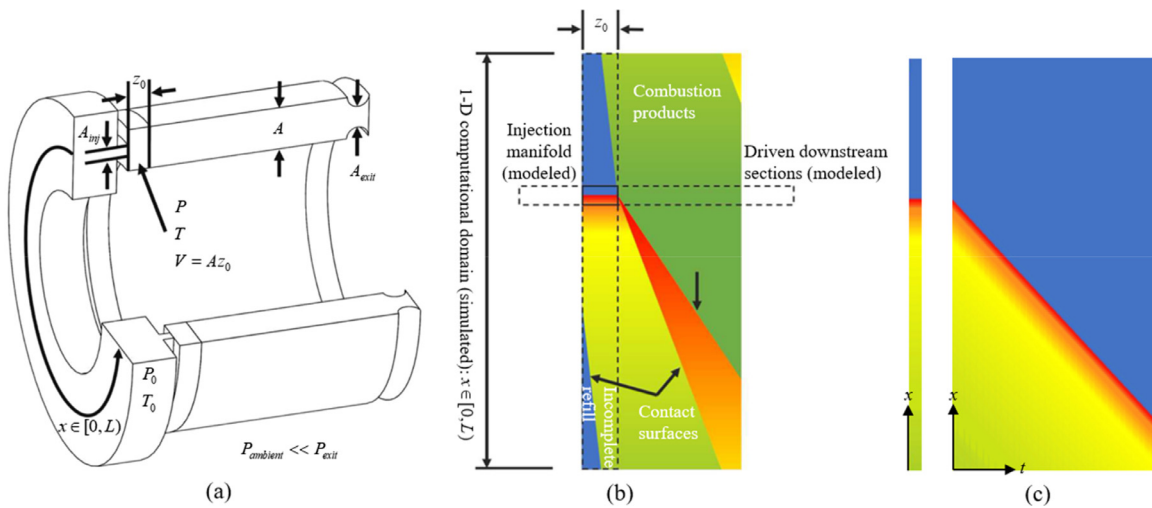


FIG. 4. Computational mode of the RDE combustor.³⁷ (a) Annular RDE combustor model, (b) simplified model of RDE combustor, and (c) spatiotemporal flow-field result.

$$E = \frac{p}{\gamma - 1} + \frac{1}{2} \rho u^2. \quad (11)$$

Furthermore, $\dot{\omega}$ indicates the chemical reaction rate, which satisfies the Arrhenius law,

$$\dot{\omega} = Da \exp \left(-E_a \left(\frac{1}{T} - \frac{1}{T_{VN}} \right) \right) \rho (1 - \lambda), \quad (12)$$

where Da is the flow Damköhler number, which is a dimensionless quantity that characterizes the relative rates of the chemical reaction and convective transport in a flow system. E_a is the activation energy, and T_{VN} is the von Neumann post-shock characteristic temperature. The α , q , β , A^+ , and A^- are the constant coefficients, while $\rho(x, t)$, $u(x, t)$, $p(x, t)$, $T(x, t)$, and $\lambda(x, t)$ represent the density, velocity, pressure, temperature, and chemical reaction progress of the flow field, respectively. Here, x is the spatial coordinate, and t is the temporal coordinate.

Equation (9) is a complex partial differential equation containing chemical reactions and more complex source terms than the 1D Euler equations for inviscid compressible flow. The equation contains mass, momentum, and energy conservations as well as chemical reaction progress. For simplicity, Eq. (9) is written in the form of

$$\frac{\partial \mathbf{U}}{\partial t} + \frac{\partial \mathbf{F}}{\partial x} = \mathbf{S}, \quad (13)$$

where vectors

$$\mathbf{U} = \begin{bmatrix} \rho \\ \rho u \\ E \\ \rho \lambda \end{bmatrix}, \quad \mathbf{F} = \begin{bmatrix} \rho u \\ \rho u^2 + p \\ u(E + p) \\ \rho u \lambda \end{bmatrix},$$

$$\mathbf{S} = \begin{bmatrix} \alpha(A^+H - A^- \sqrt{p\rho}) \\ 0 \\ \frac{\alpha}{\gamma - 1}(A^+H - TA^- \sqrt{p\rho}) + \dot{\omega}q \\ \dot{\omega} - \rho\beta H + \alpha\lambda(A^+H - A^- \sqrt{p\rho}) \end{bmatrix}$$

are functions of the variables (ρ, u, p, λ) . Among these variables, only $u(x, t)$, $p(x, t)$, and $T(x, t)$ are available for engineering measurements, and $\rho(x, t)$ can be calculated from the ideal gas equation. However, $\lambda(x, t)$ cannot be directly measured.

A fully connected PINN is built to describe the 1D RDE combustor and estimate the continuous physical fields, which has 2D inputs and 4D outputs. The input to the NN is the time and space coordinates of a specific point in the flow field (t, x) , and the output is the value corresponding to the point (ρ, u, p, λ) . Figure 5 illustrates the structure of the PINN. The left MLP network serves as a surrogate for the solution to Eq. (13). At the same time, the right physics-informed part is responsible for computing the loss functions, including losses from data measurements and the differential equation.

The $L_r(\theta)$ describes the unsupervised loss of the partial differential equation residual,

$$L_r(\theta) = \frac{1}{N_r} \sum_{i=1}^{N_r} \left\| \frac{\partial \mathbf{U}(F_\theta(x_r^i, t_r^i))}{\partial t} + \frac{\partial \mathbf{F}(F_\theta(x_r^i, t_r^i))}{\partial x} - \mathbf{S}(F_\theta(x_r^i, t_r^i)) \right\|_2^2, \quad (14)$$

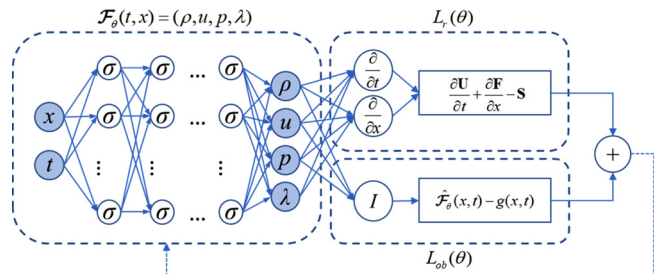


FIG. 5. Architecture of the proposed PINN. The inputs are the time and space coordinates (x, t) , and the outputs are the density, velocity, pressure, and chemical reaction progress (ρ, u, p, λ) . The physical laws are represented by partial differential equation and expressed using automatic differentiation operators.

where (x_r, t_r) is the coordinate of the sample point to calculate the residuals (called the residual point), and $F_\theta(x_r, t_r)$ is the output of the PINN at that point. Inspired by the adaptive mesh refinement (AMR)⁴³ method in CFD, the concept of adaptively refining the sampling points was borrowed from AMR to improve the sampling strategy. The pseudo-code of the adaptive residual point sampling strategy is presented as [Algorithm 1](#).

The $L_{ob}(\theta)$ is the supervised loss of the data measurements as

$$L_{ob}(\theta) = \frac{1}{N_{ob}} \sum_{i=1}^{N_{ob}} \|F_\theta(x_{ob}^i, t_{ob}^i) - g(x_{ob}^i, t_{ob}^i)\|_2^2, \quad (15)$$

where (x_{ob}, t_{ob}) is the coordinate of the observed data point, and $g(x_{ob}, t_{ob})$ is the true value at that point. The total loss is the weighted sum of $L_r(\theta)$ and $L_{ob}(\theta)$, given as

$$L(\theta) = w_r L_r(\theta) + w_{ob} L_{ob}(\theta). \quad (16)$$

The w_r and w_{ob} are the weights used to balance the interplay between the two loss terms. The PINN is trained by minimizing losses through gradient-based algorithms.

The proposed PINN model is implemented via PyTorch, an open-source deep-learning framework in Python. The selection of hyperparameters was based on references and similar applications of PINN in fluid mechanics.^{15,16,31–33,44} The Adam optimizer⁴⁵ is utilized to optimize the loss function. The weights of the loss function are set to $w_r = 1$ and $w_{ob} = 4$. A learning rate scheduler is incorporated to

ALGORITHM 1: Adaptive residual point sampling strategy.

Sample the initial residual point set P_0 randomly in the computational domain of n points.
for $i = 0$ to max_iterations **do**
 if $i \% update_freq = 0$ **then**
 (a) Compute residuals in each residual point
 (b) Retain the $n/2$ points with the largest residuals in the point set P_{i-1}
 (c) Randomly sample point set P_i^r in the computational domain of $10n$ points
 (d) Combine P_i^r and P_{i-1} to attain P_i
end for

TABLE I. Structure of the PINN model.

| Layer type | Neuron number | Activation function |
|------------|---------------|---------------------|
| Input | 2 | |
| Dense | 64 | Tanh |
| Dense | 128 | Tanh |
| Dense | 64 | Tanh |
| Output | 4 | |

accelerate convergence, which maintains a rate of 1×10^{-2} during the first 5000 iterations and decreases to 5×10^{-3} for the final 5000 iterations. Batch normalization is applied after each dense layer before the activation function to prevent saturation in the tanh activation functions. The architecture of the PINN model is an MLP network, as summarized in Table I. We also transform the output of the MLP network. Specifically, the softplus function is utilized for ρ and p because it ensures their values remain positive, while the sigmoid function is employed for λ because of its output range of 0–1. The variable u does not use any output activation function.

C. Problem setup

This section comprehensively describes the flow-field reconstruction process in the RDC. The general framework of this study is illustrated in Fig. 6, which shows the scattered observation points on the left and the high-resolution flow field reconstructed by the PINN on the right. The performed problem in the study is an inverse problem, where the equations and partial real results are known, but the overall solution of the equations is unknown. It is different from a forward problem that entails known equations with completed initial and boundary conditions. A simplified RDC model was proposed by Koch and Kutz³⁷ and is described in detail in Sec. II B. The combustor is characterized by four

independent physical variables: ρ , u , p , and λ . Among them, only ρ , u , and p are known and can be directly optimized, while no prior information is available for λ . Additionally, the data acquired by the PINN is not a continuous physical field and follows a series of fixed sensors, as shown in the left part of Fig. 6. The number of data points used for computing the partial differential equation residual is set to 4096, and the number of observation data is determined by the spatial sampling number and temporal sampling frequency, which varies with different cases. This study faces two major challenges for the PINN:

- First, the PINN is required to reconstruct the high-resolution flow field inside the RDC using sparse scattered observation data points.
- Second, the PINN must extrapolate λ without any prior information as it is optimized solely by minimizing the governing equation residuals.

The dataset is one of the crucial aspects of machine learning methods. Obtaining a detailed dataset from experiments is expensive and difficult when evaluating results. Therefore, numerical methods are employed to obtain the required data. The solutions are calculated with the open-source PDE solver PyClaw. The Haren–Lax–van Leer Riemann solver and total variation diminishing (TVD) scheme are selected to calculate the numerical fluxes, and the stepping time is in the second-order Runge–Kutta method. In the process of non-dimensionalizing all parameters, three characteristic parameters were set as the basis for this transformation: $p_0 = 1 \text{ MPa}$, $T_0 = 300 \text{ K}$, and $x_0 = 0.02 \text{ m}$. The dimensionless length is $L = 24$, the grid size is $\Delta x = 0.024$, and $\text{CFL} = 0.1$.

The other dimensionless parameters refer to gaseous kerosene (Jet-A) and oxygen-rich air ($O_{0.8}N_{1.2}$) mixture, i.e., $\gamma = 1.20$, $q = 54.5$, $T_{VN} = 6$, $Ea = 10$, and $Da = 22$. The results mainly focus on the single-wave mode sets $A^+ = 0.8$, $A^- = 0.3$, $\alpha = 0.65$, and $\beta = 0.07$.

III. RESULTS AND DISCUSSION

This section comprehensively discusses the results of flow-field reconstruction in the RDC and its influencing factors. The following

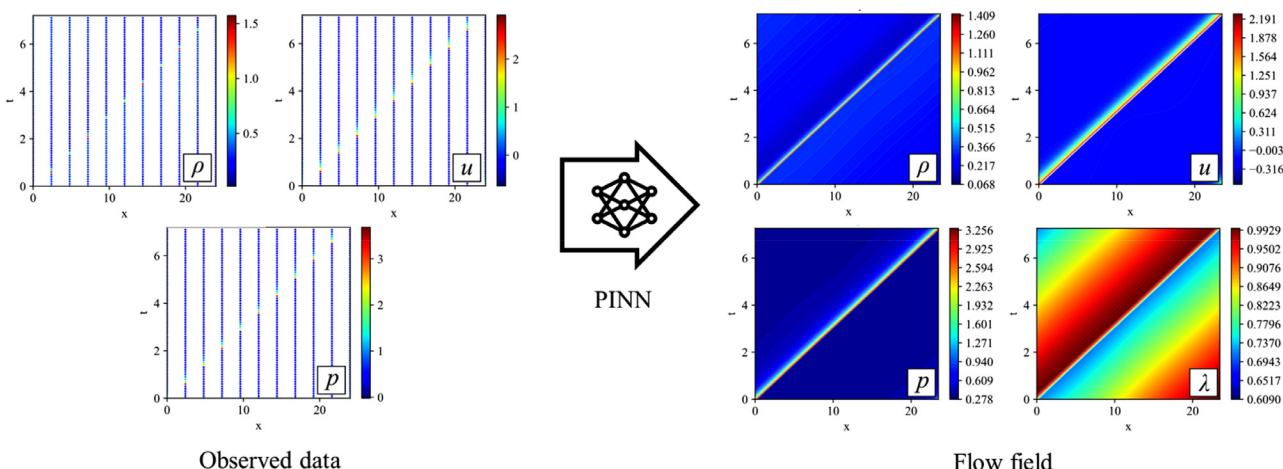


FIG. 6. Schema of the RDE combustor flow-field reconstruction problem. When using scattered observation data, the PINN will reconstruct the high-resolution flow field and extrapolate unobserved variables.

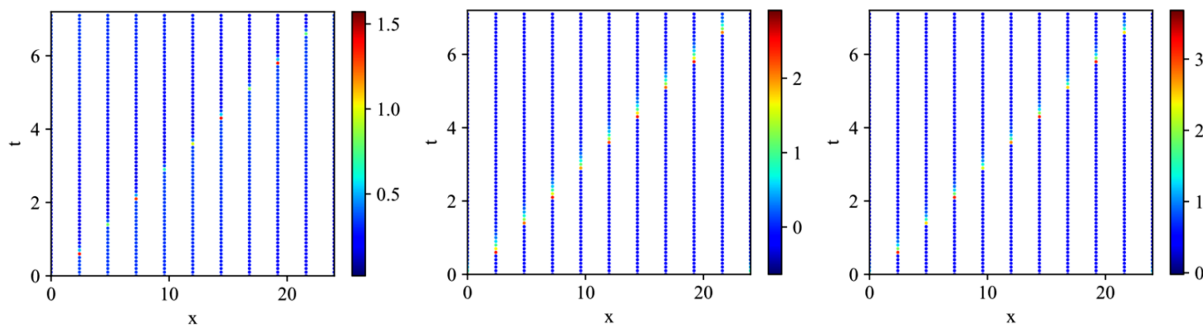


FIG. 7. Observed data from the PINN (from left to right is ρ , u , and p).

two evaluation metrics assess the accuracies of the PINN flow-field reconstruction results:

- (1) Mean absolute error (MAE): The MAE evaluates the absolute difference between the reconstructed and the original values of each sample as

$$MAE = \frac{1}{N} \sum_{i=1}^N |\mathbf{F}_\theta(\mathbf{x}^i, t^i) - g(\mathbf{x}^i, t^i)|, \quad (17)$$

where $\mathbf{F}_\theta(\mathbf{x}^i, t^i)$ denotes the PINN reconstructed flow field in each single evaluation point, $g(\mathbf{x}^i, t^i)$ denotes the ground truth flow field in each single evaluation point, and N is the number of evaluation points.

- (2) Mean relative max value error (MRME): The MRME is an adjustment of the MRE, which evaluates the relative difference between the reconstructed data and the original data of each sample, given as

$$MRE = \frac{100\%}{N} \sum_{i=1}^N \frac{|\mathbf{F}_\theta(\mathbf{x}^i, t^i) - g(\mathbf{x}^i, t^i)|}{|g(\mathbf{x}^i, t^i)|}, \quad (18)$$

where the absolute value of ground truth $|g(\mathbf{x}^i, t^i)|$ in the denominator normalizes the absolute error and characterizes the relative error. However, the $|g(\mathbf{x}^i, t^i)|$ is usually close to 0, making the expression meaningless. To overcome this issue, we adjust $|g(\mathbf{x}^i, t^i)|$ to $|\max_i(g(\mathbf{x}^i, t^i))|$, which is much greater than zero. Compared to the MRE, the MRME is better suited to evaluate the relative differences between the reconstructed data and the original data of each flow field for the samples,

$$MRME = \frac{100\%}{N} \sum_{i=1}^N \frac{|\mathbf{F}_\theta(\mathbf{x}^i, t^i) - g(\mathbf{x}^i, t^i)|}{|\max_i(g(\mathbf{x}^i, t^i))|}. \quad (19)$$

In comparison to evaluation metrics such as mean square error (MSE), root mean square error (RMSE), and mean absolute error (MAE), which reflect absolute errors, the mean relative max value error (MRME) reflects relative errors and is not affected by the unit of measurement.

A. Overview of reconstruction results

This section overviews the reconstruction results. Figure 7 illustrates the scattered observed data obtained by the PINN, showing

three notable characteristics. First, the variable λ , one of the four independent variables of the RDC, is missing from the observed data. Second, the observed data comprise only discrete points instead of representing continuous physical fields. Third, the spatial interval of the discrete data is much larger than the temporal interval due to the sensors being fixed circumferentially on the RDC. The spatial sampling number is set to ten, and the temporal sampling frequency is ten points per time unit, which is equivalent to 0.1383 MHz, per the dimensional quantities mentioned in Sec. II C. Figure 8 provides the training curve using the Adam optimizer. The optimizer successfully reduces the loss to approximately 1×10^{-4} after 10 000 epochs. The decreased loss at the 5000th iteration is due to changes in the learning rate from 1×10^{-2} to 5×10^{-3} . We also investigate the effects of the initial conditions by training ten different times with random initial variables, indicating the initial values have negligible impact on the training loss.³³

The reconstructed results are presented in Fig. 9, where the PINN accurately reconstructs the propagation process of the detonation wave from scattered observations. For the observable values ρ , u , and p , the PINN has a relatively low error with MRMEs of 2.33%, 5.38%, and 2.65%, respectively. For the unobservable value λ , the extrapolation is performed by applying the learned relationships from

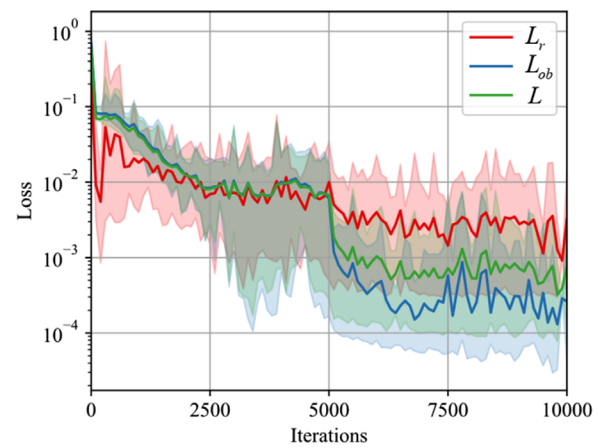


FIG. 8. Training loss curve for the PINN (shaded regions indicate the maximum and minimum of ten different training times with random initial variables). The learning rate is changed from 1×10^{-2} to 5×10^{-3} at 5000th iteration.

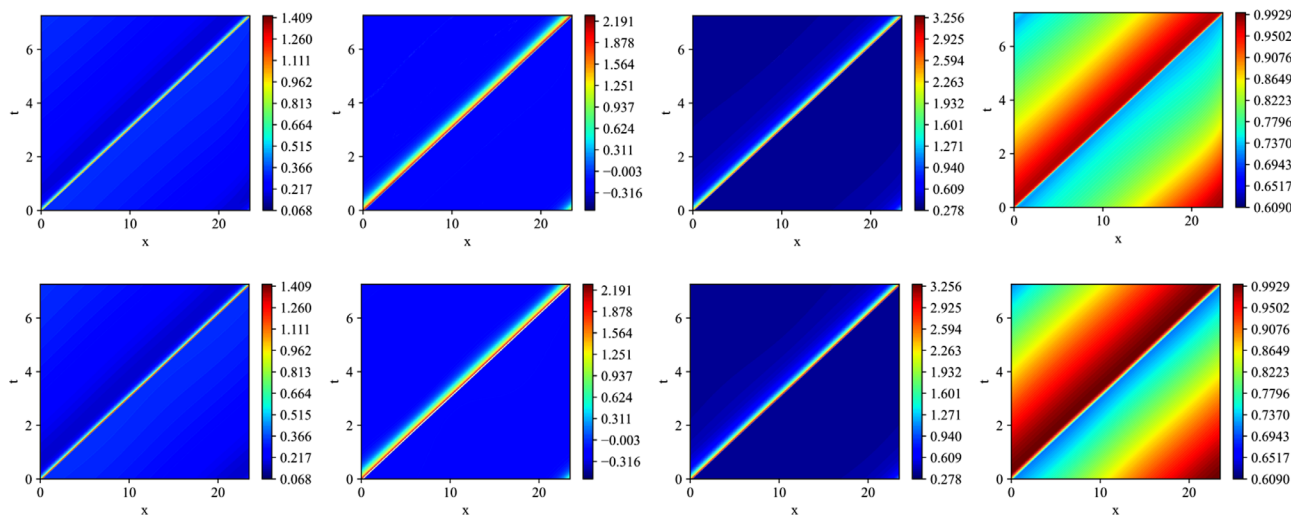


FIG. 9. PINN reconstruction results (a) and ground truth (b) based on the observed data shown in Fig. 7; subfigures from left to right are ρ , u , p , and λ . The results show that the PINN accurately reconstructs the propagation process of the detonation wave.

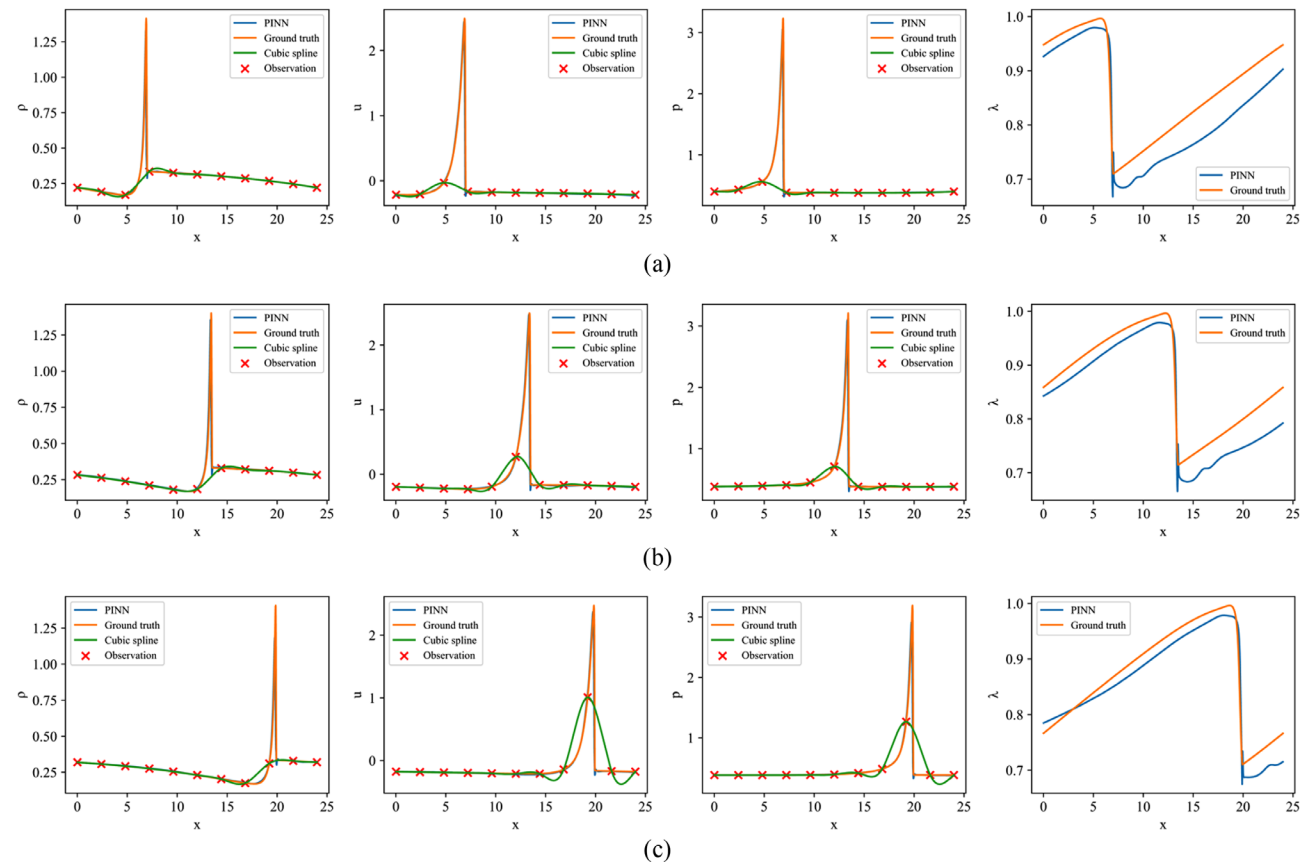


FIG. 10. Reconstruction results with time = 2 (a), 4 (b), and 6 (c). Subfigures from left to right are ρ , u , p , and λ . The PINN well captures the flow structure of the detonation wave.

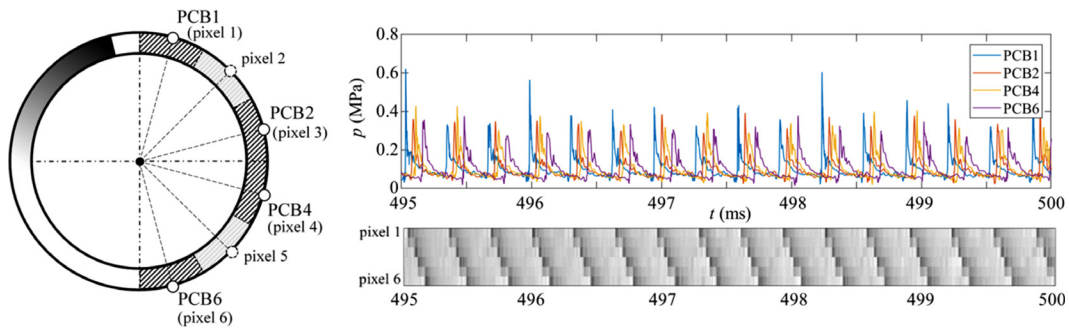


FIG. 11. Interpolation results of the pressure field based on high-frequency pressure sensor signals around the combustor.⁸

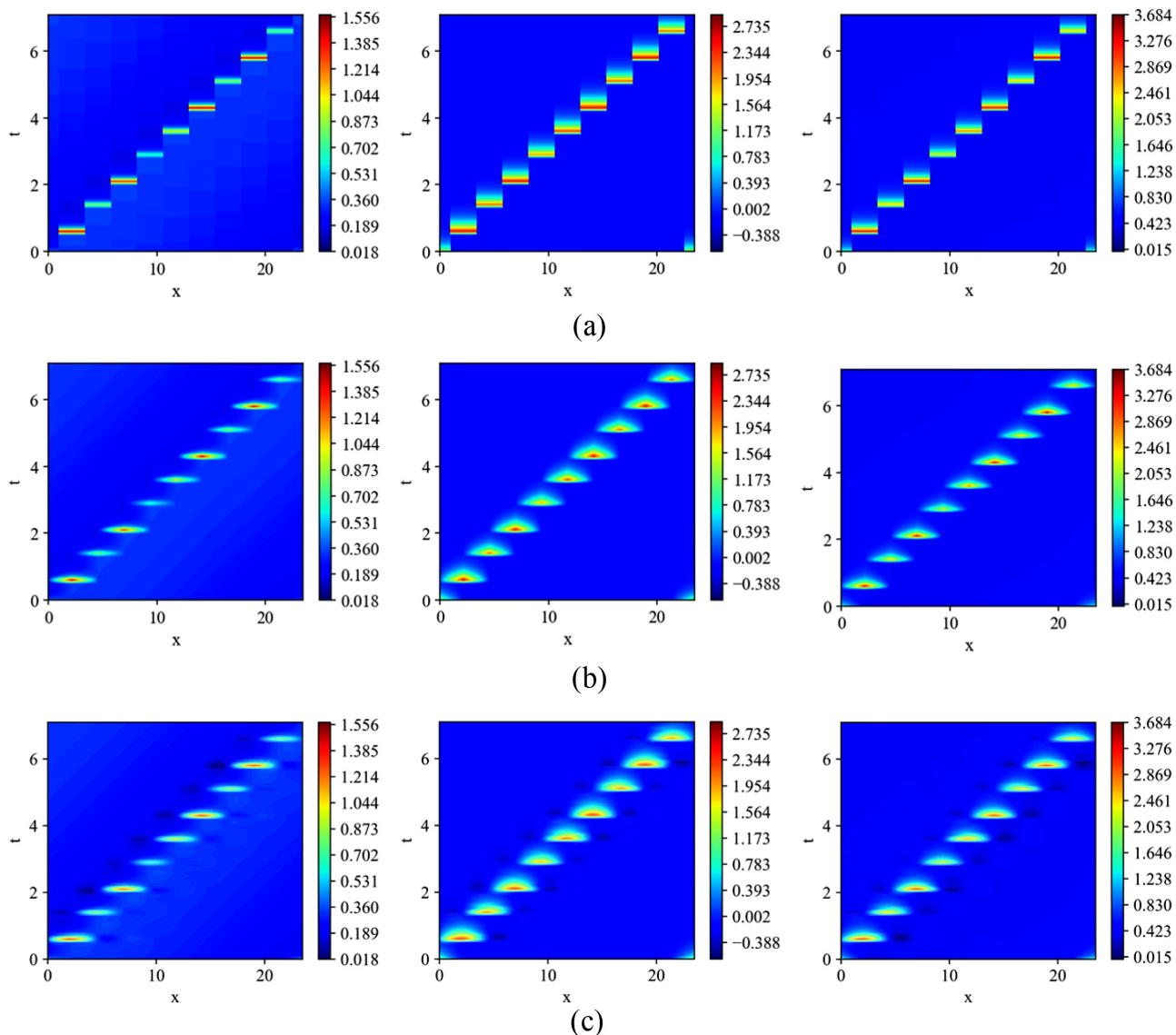


FIG. 12. Reconstruction results with nearest interpolation (a), linear interpolation (b), and cubic interpolation (c). Subfigures from left to right are ρ , u , and p . All three commonly used 2D interpolation methods fail to accurately reconstruct the continuous propagation of the detonation wave.

the observed data points and the governing equations of flow field to estimate the values of unobserved variables. The PINN accurately extrapolates the pattern of its distribution with an MRME of 6.48%. Figure 10 shows the reconstruction results of the four variables at different time instances. The PINN well captures abrupt changes in the flow variables caused by detonation wave propagation. It also captures the different distribution patterns of the flow characteristics before and after the wave. For example, the density jump before the detonation wave is sharper than the drop and slowly rebounds afterward. Overall, the PINN method can effectively characterize the specificity of flow fields on the two sides of the detonation wave.

Interpolation methods are commonly employed for processing scattered data. There are several studies on the RDE^{8,13,46} that use interpolation methods to process data. Figure 11 gives the interpolation results of the pressure field based on the high-frequency pressure sensor signal around the combustor. Due to experimental limitations, only a few sensors can be placed circumferentially around the combustor, severely impacting the interpolation results. Figure 12 shows the reconstruction results from the observed data in Fig. 7 with different 2D interpolation methods as an example. The interpolation was implemented using the open-source mathematical function library SciPy.⁴⁷ All three commonly used 2D interpolation methods fail to accurately reconstruct the continuous propagation of the detonation wave. This is attributed to the sparse spatial distribution of the observed data

relative to the temporal data, as depicted in Fig. 7. Consequently, the triangulation used in 2D interpolation of the observed data forms a large number of thin and elongated triangles (more length than width). This makes the coefficient matrix during interpolation ill-conditioned and causes poor interpolation results.⁴⁸ Additionally, triangulation-based interpolation methods only utilize geometrically adjacent points and ignore points on the path of the detonation wave, which fails to accurately reconstruct continuous detonation waves. In conclusion, the discussed 2D interpolation methods have two limitations in reconstructing the detonation wave. First, they cannot capture the physical continuity of the detonation wave propagation process. Second, they are unable to extrapolate to unobserved variables such as reaction progress λ .

B. Influence of residual sampling strategy

Training a PINN differs from conventional machine learning problems. This is because the PINN has access to the correct solution only at a few observation points, and it can only compute partial differential equation residuals and for all points. Consequently, the PINN may fail to converge due to trivial solutions acting as residual local minima. Although randomly sampling residual points works well for most cases, it may not be efficient for cases that exhibit solutions with steep gradients.⁴⁹ Detonation waves are a flow structure with a strong

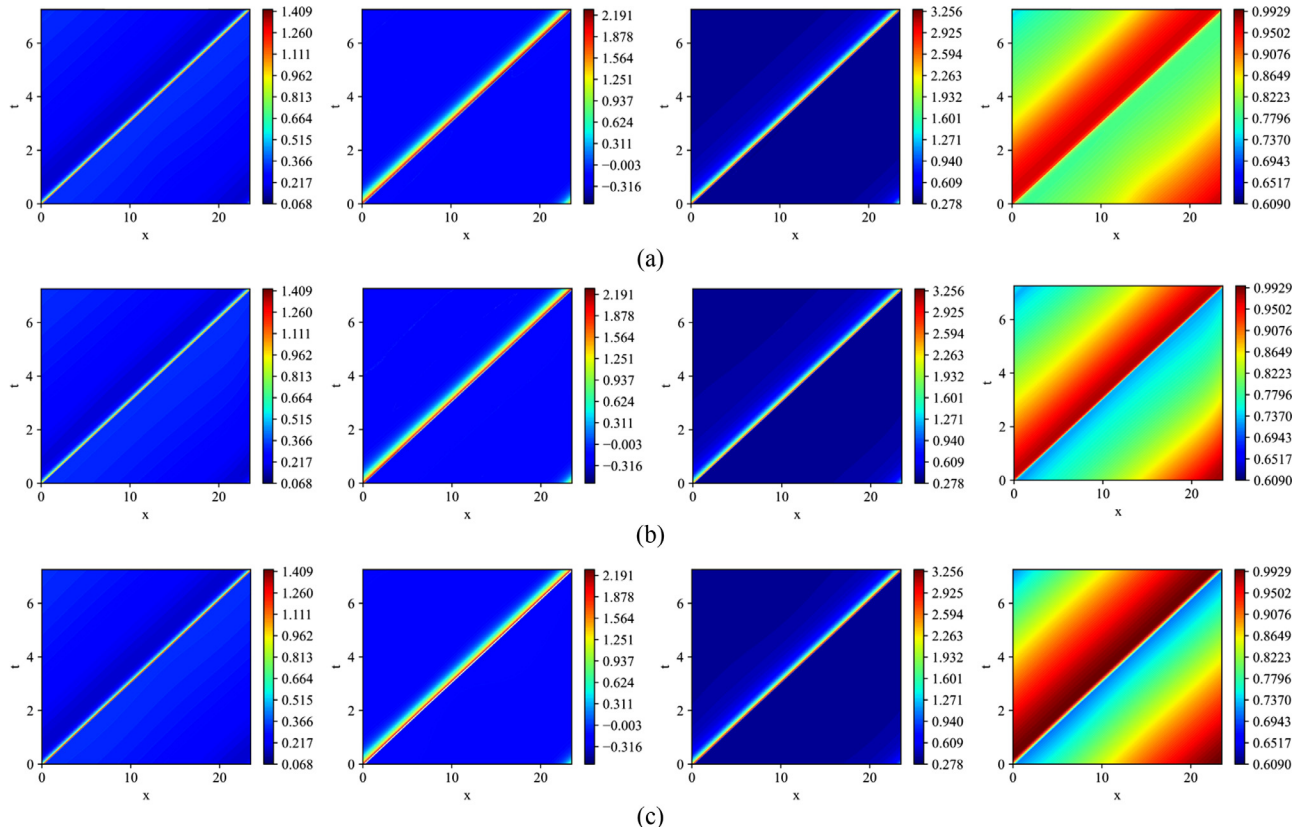


FIG. 13. Reconstruction results with random sampling strategy (a), adaptive sampling strategy (b), and ground truth (c). Subfigures from left to right are ρ , u , p , and λ . The results show that the adaptive sampling has better reconstruction, especially for peak values of the detonation wave and unobservable variable λ .

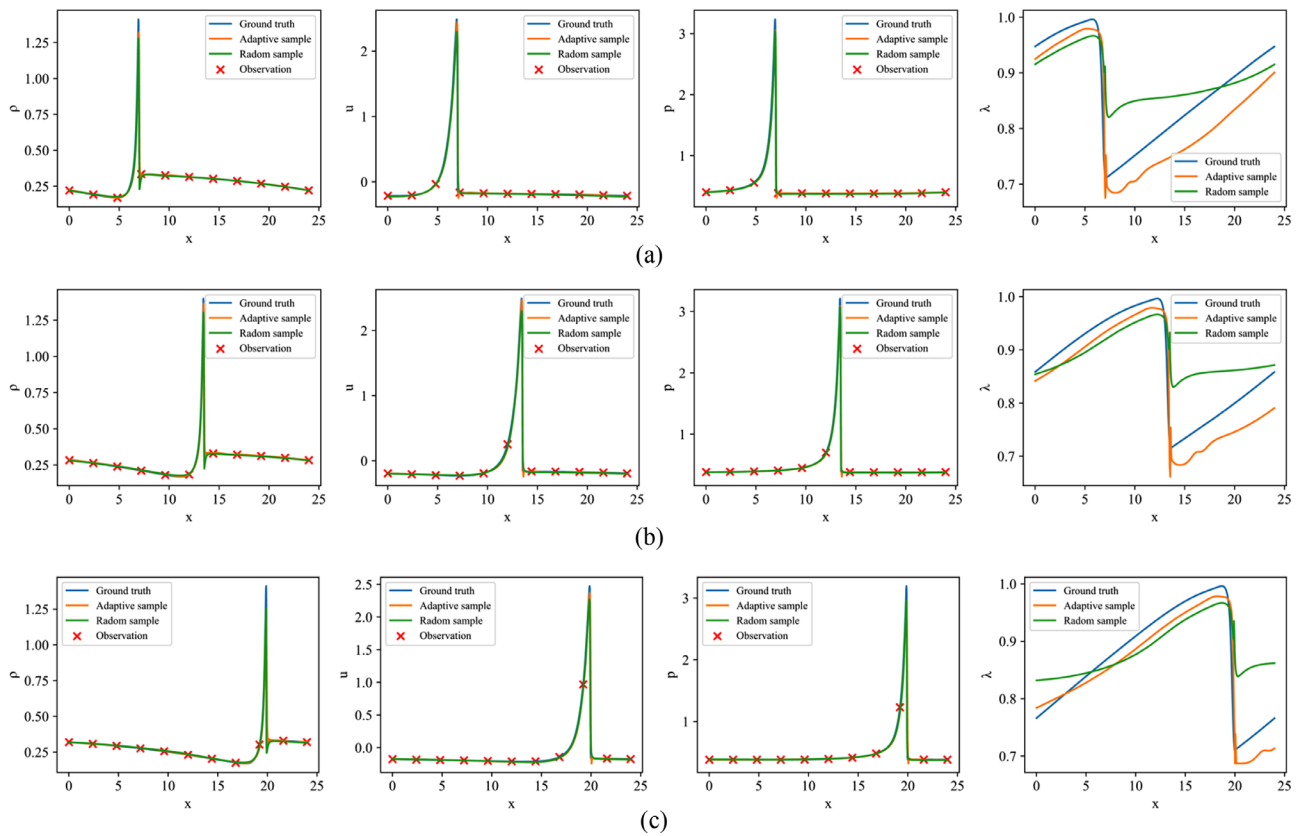


FIG. 14. Reconstruction results with time = 2 (a), 4 (b), and 6 (c). Subfigures from left to right are ρ , u , p , and λ . The results show that adaptive sampling has better reconstruction, especially for the peak values of the detonation wave and unobservable variable λ .

TABLE II. Reconstruction errors for different sampling strategies (each result is obtained by averaging ten independent runs). Adaptive sampling effectively reduces the residuals.

| | ρ | | u | | p | | λ | |
|----------|--------|------|-------|------|-------|------|-----------|------|
| | MRME | MAE | MRME | MAE | MRME | MAE | MRME | MAE |
| Random | 2.95% | 0.09 | 8.46% | 0.25 | 2.68% | 0.25 | 6.92% | 0.05 |
| Adaptive | 2.33% | 0.09 | 5.38% | 0.25 | 2.65% | 0.25 | 6.48% | 0.04 |

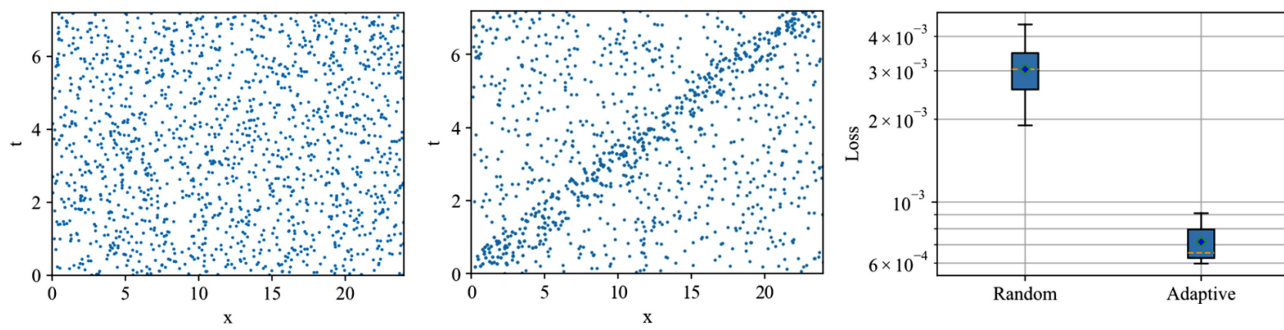


FIG. 15. Sampling points of the random (left) and adaptive (middle) sampling loss for different sampling strategies (right). Nearly all increased residual points are near the detonation wave.

gradient. Therefore, accurately reconstructing detonation waves requires more residual points placed in regions with large residuals, which is similar to adaptive mesh refinement (AMR) methods.⁴³ This method effectively solves the failure problem during PINN training and increases the accuracy.⁵⁰ Apart from generating residual points,

this method does not significantly increase the overall computational complexity. Because the computational complexity of gradient calculation is independent of the distribution of points. In this study, the update frequency of residual points was set to 100 to reduce the additional computations caused by generating residual points.

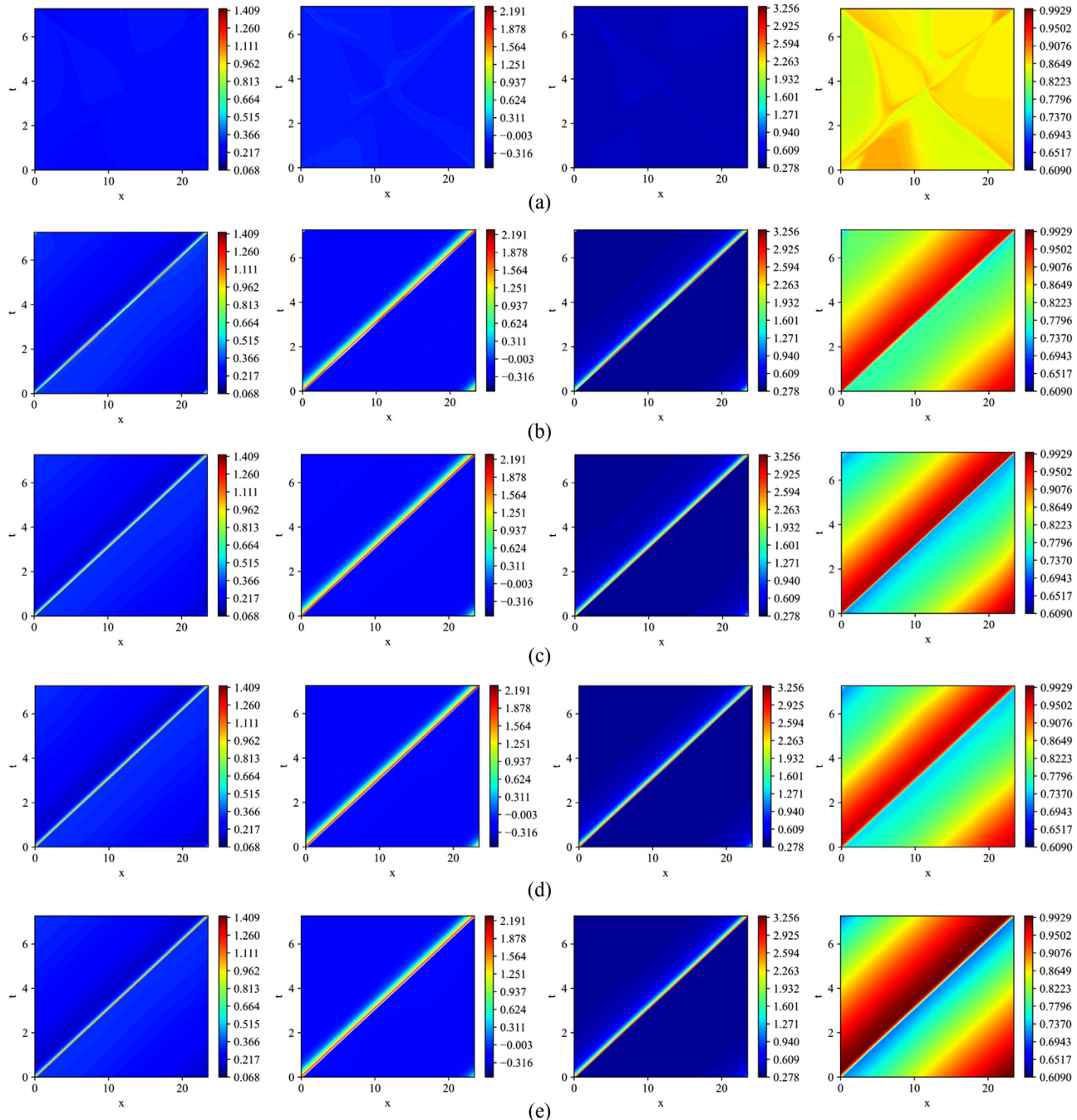


FIG. 16. Reconstruction results with sampling number = 2 (a), 6 (b), 10 (c), 14 (d), and ground truth (e). Results of sampling number = 14 is not overfit. Subfigures from left to right are ρ , u , p , and λ .

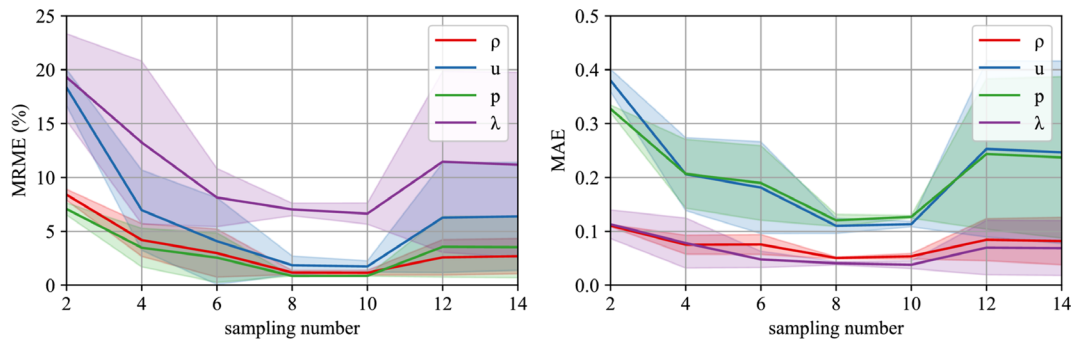


FIG. 17. Reconstruction results for different sampling numbers (shaded regions indicate the maximum and minimum of different training times, and the errors at each point are obtained by averaging five independent runs).

Algorithm 1 provides a sampling strategy that differs from conventional random sampling approaches. Analyzing the results shows improvements in the sampling strategy for the reconstruction problem. Figure 13 illustrates the reconstructed results of the random and adaptive sampling strategies. Compared to the random sampling strategy, adaptive sampling has better reconstruction, especially for the peak values of the detonation wave and unobservable variable λ . The distribution of the physical quantities at different time instances is provided in Fig. 14. The ρ , u , and p reach a steep peak at the detonation wave surface and remain stable at other positions. Moreover, λ changes smoothly at other positions and suddenly leaps after the detonation wave surface. In most positions, the sampling strategy does not affect the results. Adaptive sampling is better for ρ , u , and p in the peak region. In addition, the greater accuracy of observable value reconstruction gives the adaptive sampling better predictions for the unobservable value λ . Table II summarizes the reconstruction results for each value. Compared to the random sampling strategy, the MRME and MAE of adaptive sampling are reduced for all variables. Each sampling strategy is obtained by averaging ten independent runs.

It is theoretically impossible for the PINN to accurately fit the physical jumps caused by the shock or detonation waves because all NNs were trained using gradient-based algorithms, which would lead to an infinite gradient. However, as mentioned in Sec. II D, adaptive sampling can effectively prevent high residuals in very narrow regions. For the problem shown in Fig. 15, nearly all increased residual points are near the detonation wave. This effectively reduces the residuals [L_r in Eq. (16)] from 2×10^{-2} to 3×10^{-3} , which is nearly an order of magnitude. The reconstruction errors also decrease.

C. Influence of spatial sampling number

Sufficient observation data are needed before flow-field reconstruction. The amount of observation data indicates that the PINN model can obtain more results in a real physical field by increasing the spatial and temporal sampling densities. As noted, the temporal sampling density represents the sensor sampling frequency, and it is an inherent property of the sensor. On the other hand, the spatial sampling density represents the number of sensors. Selecting an appropriate number of sensors is crucial in experimental measurements. Too many sensors can increase the complexity and cost of the experiments, while too few sensors may reduce the reconstruction accuracy. This section investigates the influence of the amount of observation data on the accuracy of the reconstruction results by adjusting the spatial sampling density. The optimal observation data are then determined for subsequent experiments and discussions.

We adjust the spatial sampling number (number of sensors) from 2 to 14 in increments of 2. The sampling points are changed adaptively in all cases. The learning rate is 1×10^{-2} in the first 5000 iterations and 2×10^{-3} in the last 5000 iterations (10 000 iterations in total). The results are summarized in Fig. 16.

Both the MRME and MAE decrease with the spatial sampling number. These both decrease faster when the spatial sampling number is small, which then slows down for larger samplings. Figure 17 shows the reconstructed flow fields for different spatial sampling numbers, which explains the reasons for changes in the MRME and MAE. The errors at each point are obtained by averaging five independent runs. The shaded regions in Fig. 17 indicate the maximum and minimum of different training times. When the number of sensors is too small, the PINN fails to capture useful flow-field information, and the

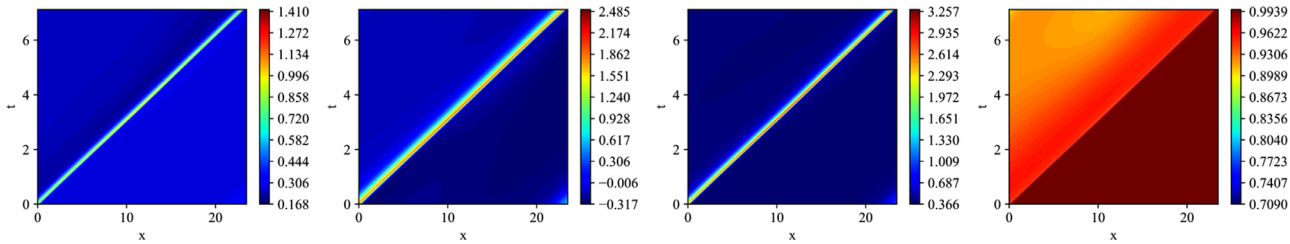


FIG. 18. Reconstruction results at sampling number = 14 when overfitting (from left to right are ρ , u , p , and λ).

reconstruction results are inaccurate. When the number of sensors reaches a certain threshold value, the PINN performs reconstruction with a nearly correct flow field that captures the propagation of the detonation wave. However, beyond a certain point, further increasing the number of sensors does not significantly improve the

reconstruction accuracy. In some cases, overfitting occurs and gives more significant errors. Figure 18 shows the result that fails to predict λ . However, due to the phenomenon of overfitting, the number of observation points cannot be too large. The flow field is reconstructed using less observed data to highlight the advantages of the PINN for

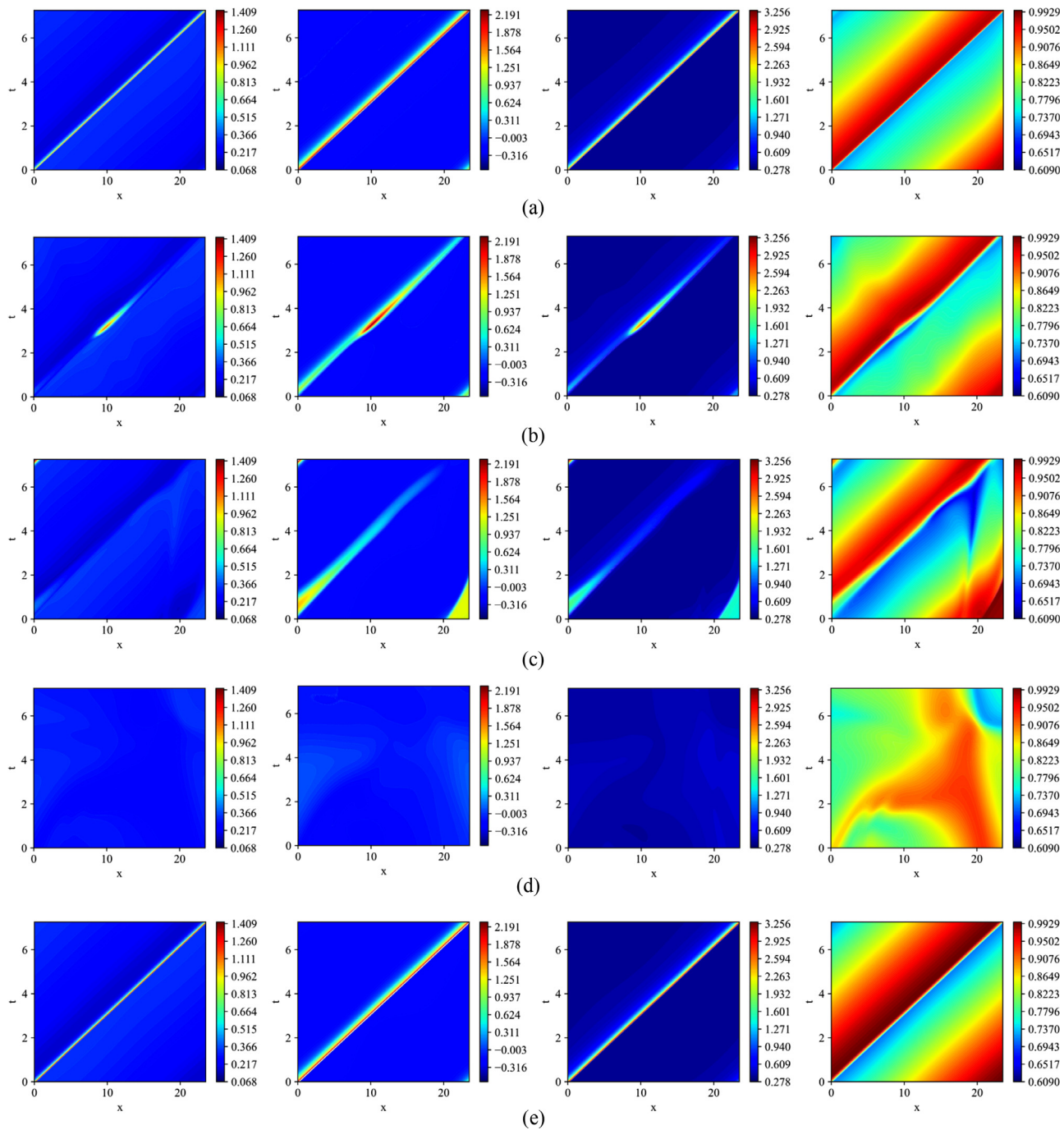


FIG. 19. Reconstruction results with sampling frequency = $1 f_0$ (a), $1/4 f_0$ (b), $1/16 f_0$ (c), $1/64 f_0$ (d), and ground truth (e). Subfigures from left to right are ρ , u , p , and λ .

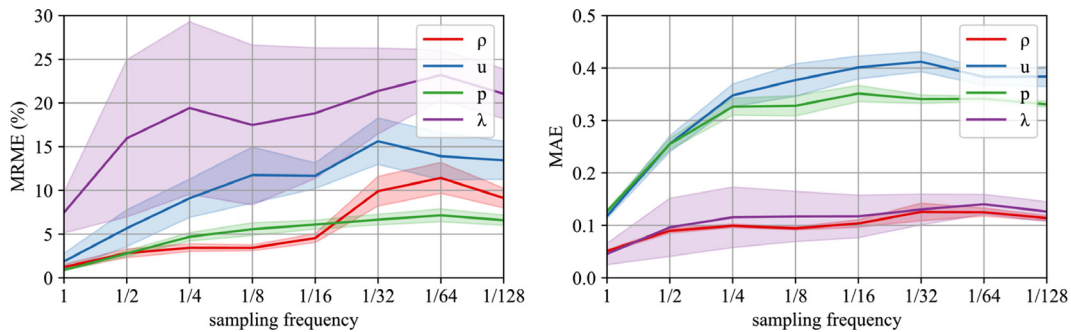


FIG. 20. Reconstruction results for different sampling frequencies (shaded regions indicate the maximum and minimum of different training times, and the errors at each point are obtained by averaging five independent runs).

solving inverse problems. The spatial sampling number is set to 10, which is chosen based on balancing accuracy and practicality.

D. Influence of temporal sampling frequency

This section focuses on the effects of the temporal sampling frequency on the prediction accuracy. The flow field is reconstructed using the PINN with different temporal sampling frequencies in Fig. 19. The temporal sampling frequency varies from 1 to 1/128 of f_0 from top to bottom. Here, f_0 represents the base temporal sampling frequency (10 points per time unit, equivalent to 0.1383 MHz) based on the dimensional quantities specified in Sec. II C. The remaining training parameters are consistent with Sec. III C. Compared with the exact solution presented in Fig. 19, the ρ , u , and p converge more readily than λ , which is similar to Sec. III C. Furthermore, reducing the sampling frequency significantly increases the errors in the predicted field. Ultimately, it becomes challenging to discern continuous detonation waves.

Figure 20 illustrates the MRME and MAE as functions of the sampling frequency. The errors are obtained by averaging five independent runs. The shaded regions indicate the maximum and

minimum of different training times. In general, the errors increase rapidly for smaller sampling frequencies. Decreasing the sampling frequency significantly reduces the prediction accuracy due to reductions in the amount of data fed into the network. Both the sampling number and frequency can affect the reconstruction results. Figure 21 provides error contour maps for different sampling numbers and frequencies, where the errors are obtained by averaging five independent runs. The sampling number and frequency do not consistently affect the reconstruction accuracy. Specifically, with an increased sampling frequency, the reconstruction accuracy continuously improves. However, the reconstruction accuracy initially increases and then decreases with larger sampling numbers. Hence, choosing a suitable spatial-temporal sampling resolution is crucial to improving the reconstruction accuracy.

E. Results of other combustion modes

This section discusses the reconstruction results of other typical combustion modes, including counter two-wave mode and unstable single-wave mode. The counter two-wave mode is a stable mode where two detonation waves propagate in opposite directions in the combustor within a certain period. The unstable single-wave mode

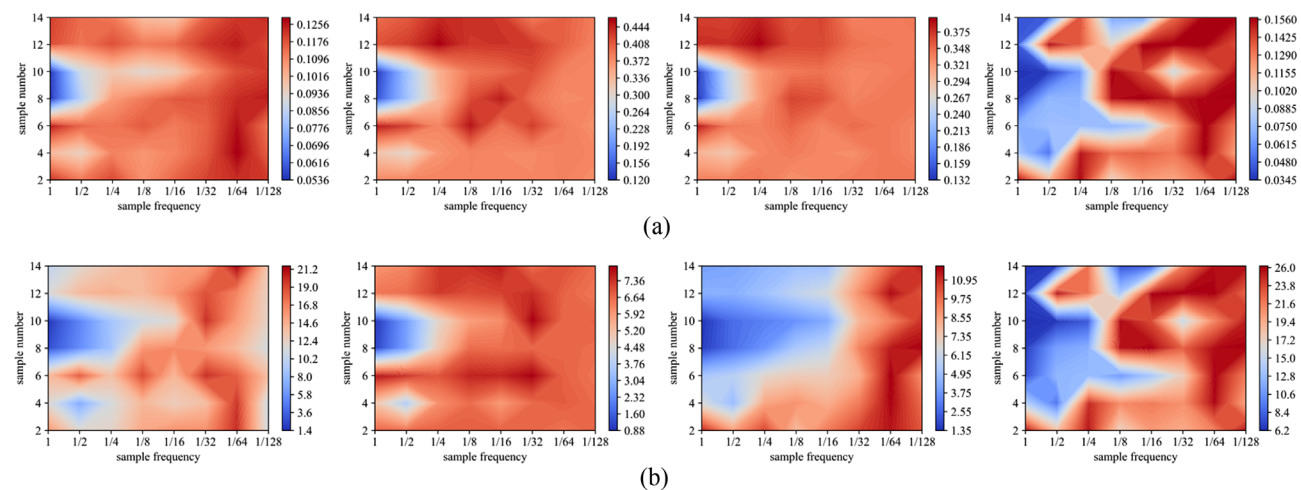


FIG. 21. MAE (a) and MRME (b) contour maps for different sampling numbers and frequencies (from left to right are ρ , u , p , and λ , and the errors at each point are obtained by averaging five independent runs).

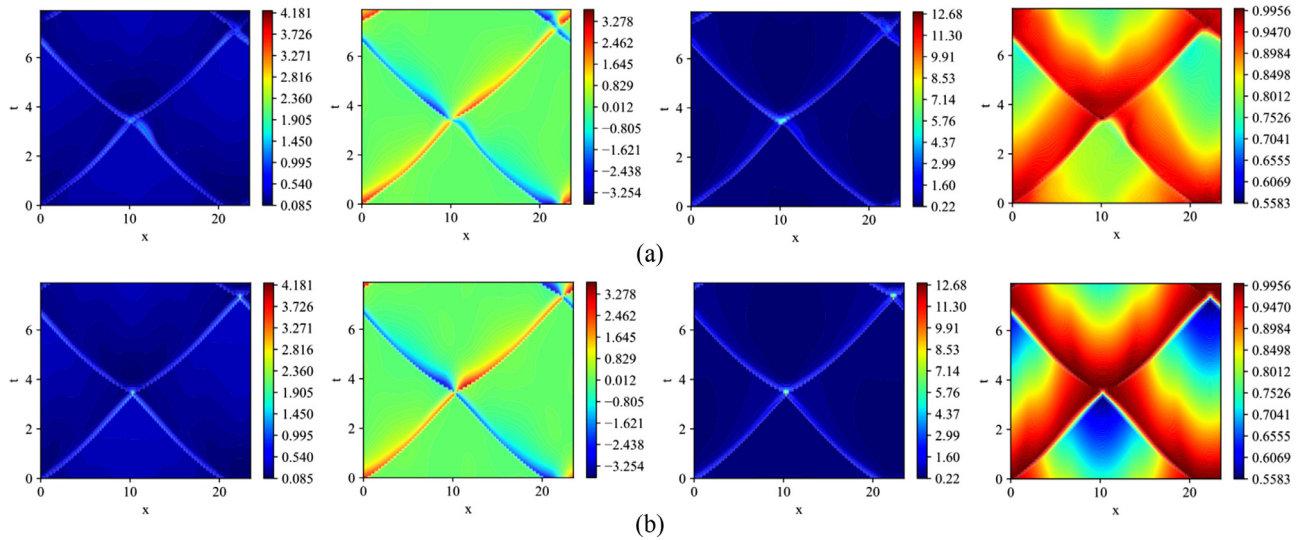


FIG. 22. Reconstruction results (a) and ground truth (b) of counter two-wave mode within one period (from left to right are ρ , u , p , and λ). The results show that the PINN accurately reconstructs the propagation process of counter two-wave mode. However, the reconstruction results around $t = 3.5$ is not as good as elsewhere, when the two waves intersect.

can be considered a special case of the single-wave mode, which is characterized by varying propagation speeds of the detonation wave. The training settings for counter two-wave mode and unstable single-wave mode are the same as Sec. III A, except that β is set to 0.09 and

0.06 to obtain the shown modes, respectively. The PINN reconstruction results for this mode are shown in Figs. 22 and 23.

The results of two complex operation modes exhibit similar trends to the single-wave results. In terms of the observable variables

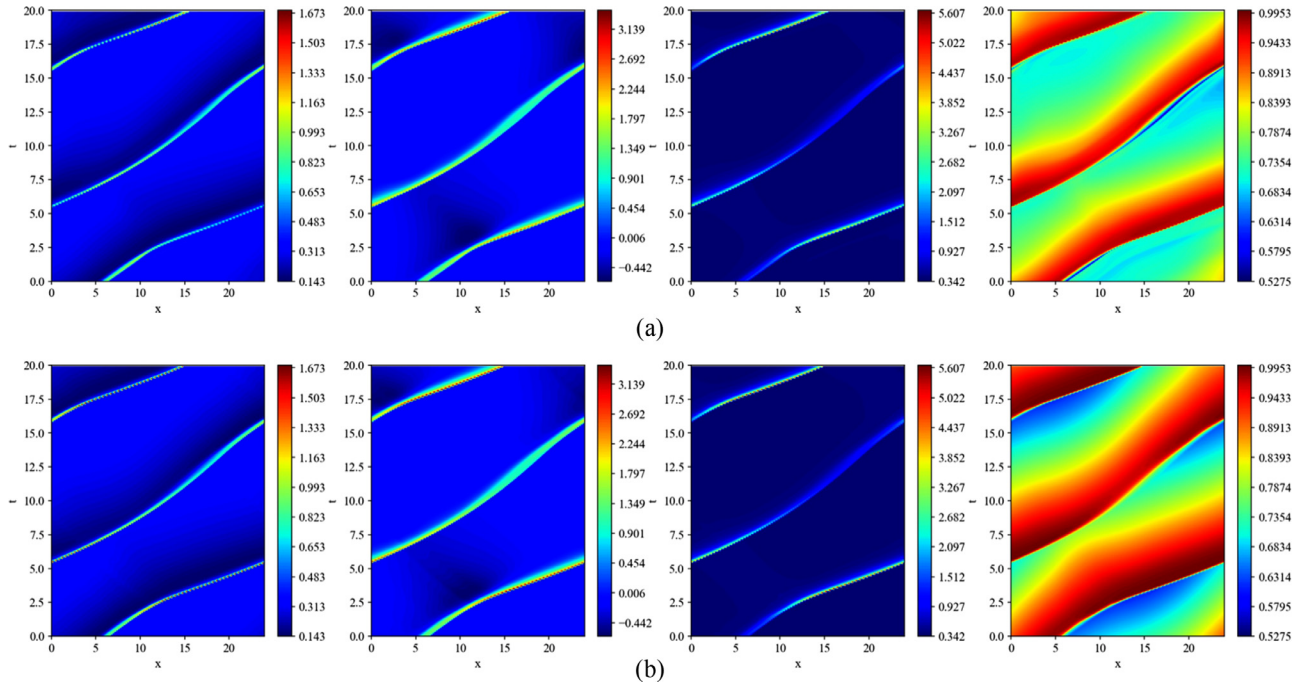


FIG. 23. Reconstruction results (a) and ground truth (b) of unstable single-wave mode within several periods (from left to right are ρ , u , p , and λ). The results show that the PINN accurately reconstructs the propagation process of unstable single-wave mode. PINN extrapolates λ with reasonable accuracy based on observable variables except for some areas with severe wave speed variations.

TABLE III. Reconstruction errors for counter two-wave mode and unstable single-wave mode (each result is obtained by averaging ten independent runs).

| | ρ | | u | | p | | λ | |
|---------------------------|--------|------|-------|------|-------|------|-----------|------|
| | MRME | MAE | MRME | MAE | MRME | MAE | MRME | MAE |
| Counter two-wave mode | 1.51% | 0.10 | 6.98% | 0.37 | 1.30% | 0.29 | 9.10% | 0.07 |
| Unstable single-wave mode | 1.84% | 0.08 | 2.89% | 0.24 | 1.68% | 0.28 | 10.11% | 0.06 |

ρ , u , and p , PINN demonstrates relatively low errors with ground truth compared to the unobservable variable λ . For the unobservable value λ , PINN still extrapolates λ with reasonable accuracy based on observable variables except for some critical areas, such as the intersection area of two waves and areas with severe wave speed variations. Table III summarizes the reconstruction results for each value. Overall, the PINN can reconstruct the results of different modes with reasonable accuracy.

IV. CONCLUSION

This paper introduces a novel RDE combustor flow-field reconstruction method based on physics-informed machine learning. The main conclusion of the proposed PINN is summarized as follows:

- (1) The designed PINN can reconstruct high-resolution flow fields in RDCs using sparsely scattered observation points. The observations include only ten sets of points with fixed spatial coordinates, representing measuring data with fixed sensors. Compared to interpolation-based methods, PINN can better capture different distribution patterns for the flow characteristics before and after the detonation wave, which matches the ground truth satisfactorily.
- (2) The designed PINN can extrapolate the missing dimensions of the flow field from the observed data and physics information. Due to limitations in experimental measurement methods, some variables in the flow field cannot be measured directly, e.g., the reaction progress λ . For the unobservable variable λ , the PINN reconstruction results still capture the critical structure of the detonation wave.
- (3) The adaptive sampling strategy significantly improves the accuracy of the detonation wave. Compared to random sampling, adaptive sampling provides better reconstruction results, especially for the peak value of the detonation wave and unobservable variable λ .
- (4) Both the sampling number and frequency significantly influence the reconstruction results. Specifically, changes in the sampling number and frequency do not consistently affect the accuracy in the same way.

Overall, the proposed method presents a practical approach for flow-field reconstruction in RDCs using physics-informed machine learning methods based on sparse and scattered observation data points with missing dimensions. This inverse problem is difficult to solve using traditional CFD methods, but the proposed PINN provides an alternative solution. To the best of our knowledge, this work is the first attempt at using PINNs to model RDCs. The proposed PINN is seen as a surrogate model of the RDC, which has promising engineering value, such as in RDC design optimization and real-time monitoring. In future work, we plan to enhance the model accuracy by

applying the attention mechanism to more precisely capture the critical structure of the detonation wave. Moreover, we will combine the PINN with experimental data to create a real surrogate model.

ACKNOWLEDGMENTS

This research was primarily supported by the National Science and Technology Major Project (No. 2017-II-0005-0030). T. Hu was supported by the Sichuan Science and Technology Program (Nos. 2021YFSY0042 and 2021YFG0360).

AUTHOR DECLARATIONS

Conflict of Interest

The authors have no conflicts to disclose.

Author Contributions

Xutun Wang: Conceptualization (equal); Investigation (equal); Methodology (equal); Software (equal); Writing – original draft (equal). **Haocheng Wen:** Conceptualization (supporting); Software (supporting); Writing – review & editing (lead). **Tong Hu:** Funding acquisition (supporting). **Bing Wang:** Conceptualization (equal); Funding acquisition (equal); Project administration (equal); Supervision (equal); Writing – review & editing (equal).

DATA AVAILABILITY

The data that support the findings of this study are available from the corresponding authors upon reasonable request.

REFERENCES

- ¹P. Wolański, “Detonative propulsion,” *Proc. Combust. Inst.* **34**(1), 125–158 (2013).
- ²K. Alhussan, M. Assad, and O. Penazkov, “Analysis of the actual thermodynamic cycle of the detonation engine,” *Appl. Therm. Eng.* **107**, 339–344 (2016).
- ³J. Zhou, F. Song, Y. Wu, S. Xu, X. Yang, P. Cheng, and Y. Li, “Investigation of pressure gain characteristics for kerosene-hot air RDE,” *Combust. Flame* **247**, 112503 (2023).
- ⁴K. Kailasanath, “Recent developments in the research on pulse detonation engines,” *AIAA J.* **41**(2), 145–159 (2003).
- ⁵J.-Y. Choi, D.-W. Kim, I.-S. Jeung, F. Ma, and V. Yang, “Cell-like structure of unstable oblique detonation wave from high-resolution numerical simulation,” *Proc. Combust. Inst.* **31**(2), 2473–2480 (2007).
- ⁶B. A. Rankin, M. L. Fotia, A. G. Naples, C. A. Stevens, J. L. Hoke, T. A. Kaemming, S. W. Theuerkauf, and F. R. Schauer, “Overview of performance, application, and analysis of rotating detonation engine technologies,” *J. Propul. Power* **33**(1), 131–143 (2017).
- ⁷T.-H. Yi, J. Lou, C. Turangan, J.-Y. Choi, and P. Wolanski, “Propulsive performance of a continuously rotating detonation engine,” *J. Propul. Power* **27**(1), 171–181 (2011).

- ⁸H. Wen, "Research on stability and pressure-gain performance of rotating detonation combustion fueled by kerosene," Ph.D. thesis (Tsinghua University, 2022).
- ⁹S. Zhou, H. Ma, C. Zhou, and N. Hu, "Experimental research on the propagation process of rotating detonation wave with a gaseous hydrocarbon mixture fuel," *Acta Astronaut.* **179**, 1–10 (2021).
- ¹⁰G. Rong, M. Cheng, Z. Sheng, X. Liu, Y. Zhang, and J. Wang, "Investigation of counter-rotating shock wave and wave direction control of hollow rotating detonation engine with Laval nozzle," *Phys. Fluids* **34**(5), 056104 (2022).
- ¹¹H. Wen, W. Wei, W. Fan, Q. Xie, and B. Wang, "On the propagation stability of droplet-laden two-phase rotating detonation waves," *Combust. Flame* **244**, 112271 (2022).
- ¹²Z. Ren and L. Zheng, "Numerical study on rotating detonation stability in two-phase kerosene-air mixture," *Combust. Flame* **231**, 111484 (2021).
- ¹³S. M. Frolov, V. S. Aksenov, V. S. Ivanov, and I. O. Shamshin, "Large-scale hydrogen-air continuous detonation combustor," *Int. J. Hydrogen Energy* **40**(3), 1616–1623 (2015).
- ¹⁴S. Cai, Z. Mao, Z. Wang, M. Yin, and G. E. Karniadakis, "Physics-informed neural networks (PINNs) for fluid mechanics: A review," *Acta Mech. Sin.* **37**(12), 1727–1738 (2021).
- ¹⁵S. Cai, Z. Wang, S. Wang, P. Perdikaris, and G. E. Karniadakis, "Physics-informed neural networks for heat transfer problems," *J. Heat Transfer* **143**(6), 060801 (2021).
- ¹⁶X. Jin, S. Cai, H. Li, and G. E. Karniadakis, "NSFnets (Navier-Stokes flow nets): Physics-informed neural networks for the incompressible Navier-Stokes equations," *J. Comput. Phys.* **426**, 109951 (2021).
- ¹⁷S. L. Brunton, B. R. Noack, and P. Koumoutsakos, "Machine learning for fluid mechanics," *Annu. Rev. Fluid Mech.* **52**(1), 477–508 (2020).
- ¹⁸R. Vinuesa and S. L. Brunton, "Enhancing computational fluid dynamics with machine learning," *Nat. Comput. Sci.* **2**(6), 358–366 (2022).
- ¹⁹Y. LeCun, Y. Bengio, and G. Hinton, "Deep learning," *Nature* **521**(7553), 436–444 (2015).
- ²⁰B. Mahesh, "Machine learning algorithms—A review," *Int. J. Sci. Res.* **9**, 381–386 (2020).
- ²¹I. H. Sarker, "Machine learning: Algorithms, real-world applications and research directions," *SN Comput. Sci.* **2**(3), 160 (2021).
- ²²S. Ekins, A. C. Puhl, K. M. Zorn, T. R. Lane, D. P. Russo, J. J. Klein, A. J. Hickey, and A. M. Clark, "Exploiting machine learning for end-to-end drug discovery and development," *Nat. Mater.* **18**(5), 435–441 (2019).
- ²³M. Jiang, H. Wu, Y. An, T. Hou, Q. Chang, L. Huang, J. Li, R. Su, and P. Zhou, "Fiber laser development enabled by machine learning: Review and prospect," *Photonix* **3**(1), 16 (2022).
- ²⁴Z. Ahmed, K. Mohamed, S. Zeeshan, and X. Dong, "Artificial intelligence with multi-functional machine learning platform development for better healthcare and precision medicine," *Database* **2020**, baaa010.
- ²⁵E. Abbasi, M. R. A. Moghaddam, and E. Kowsari, "A systematic and critical review on development of machine learning based-ensemble models for prediction of adsorption process efficiency," *J. Cleaner Prod.* **379**, 134588 (2022).
- ²⁶M. M. Moore, E. Slonimsky, A. D. Long, R. W. Sze, and R. S. Iyer, "Machine learning concepts, concerns and opportunities for a pediatric radiologist," *Pediatr. Radiol.* **49**(4), 509–516 (2019).
- ²⁷Y.-A. Hsieh and Y. J. Tsai, "Machine learning for crack detection: Review and model performance comparison," *J. Comput. Civ. Eng.* **34**(5), 04020038 (2020).
- ²⁸J. Wei, X. Chu, X.-Y. Sun, K. Xu, H.-X. Deng, J. Chen, Z. Wei, and M. Lei, "Machine learning in materials science," *InfoMat* **1**(3), 338–358 (2019).
- ²⁹G. E. Karniadakis, I. G. Kevrekidis, L. Lu, P. Perdikaris, S. Wang, and L. Yang, "Physics-informed machine learning," *Nat. Rev. Phys.* **3**(6), 422–440 (2021).
- ³⁰M. Raissi, P. Perdikaris, and G. E. Karniadakis, "Physics-informed neural networks: A deep learning framework for solving forward and inverse problems involving nonlinear partial differential equations," *J. Comput. Phys.* **378**, 686–707 (2019).
- ³¹S. Cai, Z. Wang, F. Fuest, Y. J. Jeon, C. Gray, and G. E. Karniadakis, "Flow over an espresso cup: Inferring 3-D velocity and pressure fields from tomographic background oriented Schlieren via physics-informed neural networks," *J. Fluid Mech.* **915**, A102 (2021).
- ³²M. Raissi, A. Yazdani, and G. E. Karniadakis, "Hidden fluid mechanics: Learning velocity and pressure fields from flow visualizations," *Science* **367**(6481), 1026–1030 (2020).
- ³³H. Wang, Y. Liu, and S. Wang, "Dense velocity reconstruction from particle image velocimetry/particle tracking velocimetry using a physics-informed neural network," *Phys. Fluids* **34**(1), 017116 (2022).
- ³⁴C. Yan, S. Xu, Z. Sun, D. Guo, S. Ju, R. Huang, and G. Yang, "Exploring hidden flow structures from sparse data through deep-learning-strengthened proper orthogonal decomposition," *Phys. Fluids* **35**(3), 037119 (2023).
- ³⁵M. Delcey, Y. Cheney, and S. Kiesgen de Richter, "Physics-informed neural networks for gravity currents reconstruction from limited data," *Phys. Fluids* **35**(2), 027124 (2023).
- ³⁶Z. Yang, H. Yang, and Z. Yin, "Super-resolution reconstruction for the three-dimensional turbulence flows with a back-projection network," *Phys. Fluids* **35**(5), 055123 (2023).
- ³⁷J. Koch and J. N. Kutz, "Modeling thermodynamic trends of rotating detonation engines," *Phys. Fluids* **32**(12), 126102 (2020).
- ³⁸I. Goodfellow, Y. Bengio, and A. Courville, *Deep Learning* (MIT Press, 2016).
- ³⁹K. Hornik, M. Stinchcombe, and H. White, "Multilayer feedforward networks are universal approximators," *Neural Networks* **2**(5), 359–366 (1989).
- ⁴⁰A. G. Baydin, B. A. Pearlmutter, A. A. Radul, and J. M. Siskind, "Automatic differentiation in machine learning: A survey," [arXiv:1502.05767](https://arxiv.org/abs/1502.05767) (2018).
- ⁴¹V. Anand and E. Gutmark, "Rotating detonation combustors and their similarities to rocket instabilities," *Prog. Energy Combust. Sci.* **73**, 182–234 (2019).
- ⁴²R. Zhou and J.-P. Wang, "Numerical investigation of flow particle paths and thermodynamic performance of continuously rotating detonation engines," *Combust. Flame* **159**(12), 3632–3645 (2012).
- ⁴³R. Deiterding, "Adaptive mesh refinement—Theory and applications," in *Proceedings of the Chicago Workshop on Adaptive Mesh Refinement Methods, Sept. 3–5, 2003* (Springer, 2005), Vol. 41, see <http://link.springer.com/10.1007/b138538>.
- ⁴⁴S. Markidis, "The old and the new: Can physics-informed deep-learning replace traditional linear solvers?" *Front. Big Data* **4** (2021).
- ⁴⁵D. P. Kingma and J. Ba, "Adam: A method for stochastic optimization," [arXiv:1412.6980](https://arxiv.org/abs/1412.6980) (2017).
- ⁴⁶H. Wen, Q. Xie, and B. Wang, "Propagation behaviors of rotating detonation in an obround combustor," *Combust. Flame* **210**, 389–398 (2019).
- ⁴⁷P. Virtanen, R. Gommers, T. E. Oliphant, M. Haberland, T. Reddy, D. Cournapeau, E. Burovski, P. Peterson, W. Weckesser, J. Bright, S. J. Van Der Walt, M. Brett, J. Wilson, K. J. Millman, N. Mayorov, A. R. J. Nelson, E. Jones, R. Kern, E. Larson, C. J. Carey, I. Polat, Y. Feng, E. W. Moore, J. VanderPlas, D. Laxalde, J. Perktold, R. Cimrman, I. Henriksen, E. A. Quintero, C. R. Harris, A. M. Archibald, A. H. Ribeiro, F. Pedregosa, P. Van Mulbregt, A. Vijaykumar, A. P. Bardelli, A. Rothberg, A. Hilboll, A. Kloekner, A. Scopatz, A. Lee, A. Rokem, C. N. Woods, C. Fulton, C. Masson, C. Häggström, C. Fitzgerald, D. A. Nicholson, D. R. Hagen, D. V. Pasechnik, E. Olivetti, E. Martin, E. Wieser, F. Silva, F. Lenders, F. Wilhelm, G. Young, G. A. Price, G.-L. Ingold, G. E. Allen, G. R. Lee, H. Audren, I. Probst, J. P. Dietrich, J. Silterra, J. T. Webber, J. Slavić, J. Nothman, J. Buchner, J. Kulick, J. L. Schönberger, J. V. De Miranda Cardoso, J. Reimer, J. Harrington, J. L. C. Rodriguez, J. Nunez-Iglesias, J. Kuczynski, K. Tritz, M. Thoma, M. Newville, M. Kümmeler, M. Bolingbroke, M. Tartre, M. Pak, N. J. Smith, N. Nowaczyk, N. Shebanov, O. Pavlyk, P. A. Brodtkorb, P. Lee, R. T. McGibbon, R. Feldbauer, S. Lewis, S. Tygier, S. Sievert, S. Vigna, S. Peterson, S. More, T. Pudlik, T. Oshima, T. J. Pingel, T. P. Robitaille, T. Spura, T. R. Jones, T. Cera, T. Leslie, T. Zito, T. Krauss, U. Upadhyay, Y. O. Halchenko, Y. Vázquez-Baeza, and SciPy 1.0 Contributors, "SciPy 1.0: Fundamental algorithms for scientific computing in Python," *Nat. Methods* **17**(3), 261–272 (2020).
- ⁴⁸I. Amidror, "Scattered data interpolation methods for electronic imaging systems: A survey," *J. Electron. Imaging* **11**(2), 157 (2002).
- ⁴⁹L. Lu, X. Meng, Z. Mao, and G. E. Karniadakis, "DeepXDE: A deep learning library for solving differential equations," *SIAM Rev.* **63**(1), 208–228 (2021).
- ⁵⁰A. Daw, J. Bu, S. Wang, P. Perdikaris, and A. Karpatne, "Mitigating propagation failures in PINNs using evolutionary sampling," [arXiv:2207.02338](https://arxiv.org/abs/2207.02338) (2022).